

# DISCOVERY OF ROTATIONAL MODULATIONS IN THE PLANETARY-MASS COMPANION 2M1207B: A SLOW ROTATION PERIOD AND CLOUD HEIGHT IN A LOW GRAVITY ATMOSPHERE

YIFAN ZHOU<sup>1</sup>, DÁNIEL APAI<sup>1,2,3</sup>, GLENN SCHNEIDER<sup>1</sup>, MARK S. MARLEY<sup>4</sup>

*Draft version September 17, 2015*

## ABSTRACT

Rotational modulations of brown dwarfs have recently provided powerful constraints on the properties of ultra-cool atmospheres, including longitudinal and vertical cloud structures and cloud evolution. Furthermore, detection of periodic light curve can directly probe the rotational periods of ultra-cool objects.

We present here, for the first time, time-resolved high-precision photometric measurements of a planetary-mass companion, 2MASS1207b, to a brown dwarf primary. Using HST/WFC3 observation and point spread function fitting photometry with two spacecraft roll angles, we detect photometric modulations in the light curve. The amplitudes are 1.45% in the F125W and 0.92% in the F160W filters; we find a consistent period of  $10.2^{+0.9}_{-0.8}$  h and similar phase in both bands by fitting sinusoids to the light curves. **The relative amplitudes in the two filters are very similar to that found in a recent study of a field (high-gravity) L-dwarf, suggesting that the cloud structures that introduce the photometric modulations are similar in high- and low-gravity objects.** Importantly, our study also measures, for the first time, the rotational period for directly an imaged planetary-mass companion.

*Subject headings:* brown dwarfs – planets and satellites: atmospheres – planets and satellites: individual (2M1207 b) – techniques: photometric

## 1. INTRODUCTION

Presence of condensate clouds is one the most unique and essential features of the ultra-cool atmosphere of direct imaged exoplanet and brown dwarfs. The studies of formation and properties of condensate clouds (e.g. Ackerman & Marley 2001; Burrows et al. 2006; Helling et al. 2008; Allard et al. 2012) have achieved great improvement in understanding the cloud behavior across different spectral types, especially in the explanation of L-T transition (e.g. Burrows et al. 2006; Marley et al. 2010). Surface gravity is suggested to be another key parameters in defining cloud structures besides spectral type. Low surface gravity objects (e.g. HR8799 bcd, Marois et al. (2008), 2M1207 b, Chauvin et al. (2005)) show significantly redder color compared to their spectral type matched brown dwarfs. The anomalous colors of low surface gravity objects are best explained by the existence of thick clouds (Barman et al. 2011; Skemer et al. 2011, 2012). However, due to lack of observational constraint, the dependence of cloud properties on surface gravity is not very well modeled.

Intensity modulations introduced by heterogeneous clouds can be directly observed and studied via time resolved observation and rotational mapping. These techniques isolate the effect of cloud properties and obtained great success in determining the rotation period and unveiling the structures of the atmosphere of brown dwarfs (e.g. Apai et al. 2013; Buenzli et al. 2012, 2015; Burgasser

et al. 2013; Radigan et al. 2012; Yang et al. 2014; Metchev et al. 2015). Kostov & Apai (2013) demonstrated the great potential of these techniques in the study of the cloud properties of direct imaged exoplanets and planetary mass companions. However, high contrast magnifies the challenges for direct imaged exoplanets and planetary mass companions to acquire high-precision light curves comparing to brown dwarfs.

2M1207 b is a planetary mass companion that has mass of  $\sim 2.3 - 4.8 M_{\text{Jup}}$  (Barman et al. 2011) and an angular separation of  $0.78''$  to its host 2M1207 A, an M8 brown dwarf. Moderate contrast (6.7 mag in J-band, Mohanty et al. 2007) makes it one the most feasible planetary mass companions for high-precision time-resolved observation.

In this *Letter* we present the first, high-cadence, high-precision, time-resolved *Hubble Space Telescope* (HST) photometric time series of 2M1207 b, a directly imaged planet or planetary-mass object. We successfully detect rotational modulation and measure the amplitudes in two bands and determine the rotational period.

## 2. OBSERVATION

We obtained direct images of the 2M1207A+b system on UT 2014 April 11 from 08:07:47 to 16:53:18 using HST and its Wide Field Camera 3 (WFC3, pixel scale  $\sim 0.13''$ , Kimble et al. 2008) in the frame of the HST Proposal GO-13418 (PI: D. Apai). We acquired the observations in filters F125W ( $\lambda_{\text{pivot}} = 1245.9$  nm, full width at half maximum (FWHM) = 301.5 nm) and F160W ( $\lambda_{\text{pivot}} = 1540.52$ , FWHM = 287.9 nm), roughly corresponding to the J and H bands. We used the  $256 \times 256$  pixels sub-array mode to avoid memory dumps during the observations. In order to provide a near-continuous coverage for detecting modulations we observed the 2M1207 system in 6 consecutive HST orbits, obtaining data with cadence of  $\sim 1.5$  minutes over a base-

<sup>1</sup> Department of Astronomy/Steward Observatory, The University of Arizona, 933 N. Cherry Ave., Tucson, AZ, 85721, USA, yifzhou@email.arizona.edu

<sup>2</sup> Lunar and Planetary Laboratory, The University of Arizona, 1640 E. University Blvd., Tucson, AZ 85718, USA

<sup>3</sup> Earths in Other Solar Systems Team, NASA Nexus for Exoplanet System Science

<sup>4</sup> NASA Ames Research Center, Naval Air Station, Moffett Field, Mountain View, CA 94035, USA

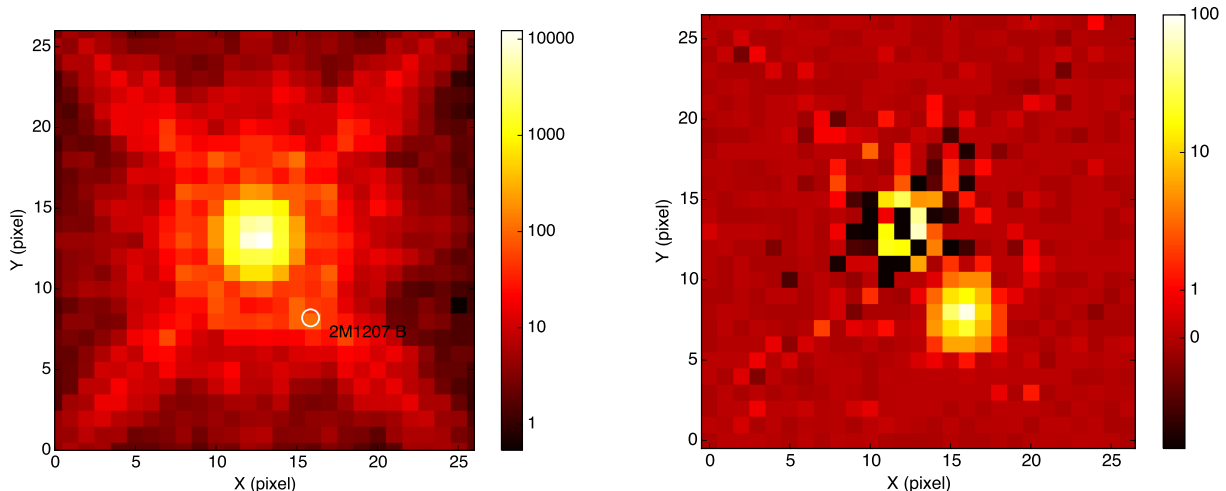


FIG. 1.— WFC3 F160W images for 2M1207 system. *Upper panel:* original image, the position of 2M1207b is indicated using white circle. *Lower panel:* residual image – after the subtraction of the hybrid PSF, 2M1207 B is detected at a high significant level.

line of 8 hours and 40 minutes. The observations were interrupted by 58 minutes long Earth occultations every 94 minutes.

The observations applied space craft rolls between each two orbits to allow roll-subtraction of the primary (e.g. Song et al. 2006). The telescope roll angles for orbit 1, 3, and 5, and those for 2, 4, and 6 differ by  $25^\circ$ . At the separation of 2M1207 b, this angle difference corresponds to a displacement of  $0.34''$ , or 2.75 and 2.30 resolution elements in F125W and F160W, respectively. In each orbit we took 8 SPARS10 exposure sequence with NSAMP=10, alternating between F160W and F125W filters, with 2–3 identical exposures in one exposure sequence. To improve sampling and reduce the risk that point spread function (PSF) lays on bad pixels, we applied a 4-point dither pattern with differential “X/Y” offsets of  $1.375''$  in the detector frame, providing optimal non-integral (half pixel) stepping of 10.5 and 8.5 pixels in F125W and F160W, respectively. Over the 6 orbits, we obtained 70 images with 10 non-destructive read-outs in F125W and 64 images in F160W with exposure time of 88.4 s for both filters.

### 3. DATA REDUCTION

#### 3.1. Photometry

We start the reduction from the `flt` files produced by the WFC3’s `calwfc3` pipeline. We do not opt to use `ima` files that contain all non-destructive read-outs, because these provided less information on 2M1207A, which saturated after the first few samples. The `flt` files are results of basic calibration, including dark current correction, non-linearity correction, flat field correction, as well as up-the-ramp fit on the non-destructive read-outs. From the beginning, pixels with data quality flags “bad detector pixels”, “unstable response”, and “bad or uncertain flat value” are masked out and excluded from further analysis as suggested by previous transit exoplanet spectroscopic observations (e.g. Berta et al. 2012; Kreidberg et al. 2014).

One major challenge of high contrast imaging observation using WFC3/IR is significant under-sampling of the detector. 2M1207 A and b are only separated by

$\sim 6$  pixels or  $\sim 5$  FWHM of the PSF. When applying roll subtraction, notable artifacts are generated by image shifting and interpolation. On the other hand, *Tiny Tim* PSF simulator (Krist 1995) offers a solution by providing Nyquist or better sampled PSF, but systematic errors of *Tiny Tim* PSF for WFC3 limits its ability in high precision photometry (Biretta 2014). However, we are able to fully characterize the difference of model and observed PSFs with 6 orbits time-resolved observation data. To obtain robust *Tiny Tim* PSF photometry, we design a 2-round PSF fitting strategy: 1. calculating correction map for *Tiny Tim*; 2. hybrid PSF photometry.

For both of 2 rounds, we use *Tiny Tim* to calculate  $10\times$  over-sampled model PSFs based on the filters, the spectra (Bonnetfoy et al. 2014; Patience et al. 2010), the telescope’s actual focus, and the telescope jitter. We use the set of *Tiny Tim* parameters provided by Biretta (2014) to improve modeling the cold mask, OTA spikes, and the coma. The focus parameters are calculated using the model listed on the STScI website<sup>5</sup>. To register the *Tiny Tim* PSF to the observed PSF of 2M1207 A, we move the over-sampled PSF on a coordinate grid (grid size=0.001 pixel) using cubic interpolation, and search for the position that minimizes the rms difference of the observed and re-binned *Tiny Tim* PSFs over a region centered on 2M1207 b excluded. Then we introduce another *Tiny Tim* PSF for 2M1207 b and fit the position of 2M1207 b and the scales of the *Tiny Tim* PSFs of 2M1207 A and b simultaneously with least square optimization. From the first round fit, we discover that the difference of observed PSFs and model PSFs are very stable for given PSF positions. Therefore, at the end of the first round PSF fitting, we derive 8 (2 roll angles  $\times$  4 dithering positions) correction maps for each filter:

$$\text{Corr} = \text{Median}(\text{PSF}_{\text{obs.}} - \text{PSF}_{\text{model}}) \quad (1)$$

where  $\text{PSF}_{\text{model}}$  is a combination of two *Tiny Tim* PSFs for 2M1207 A and b. In the second round, we combine the correction term linearly with the two *Tiny Tim* PSFs to generate hybrid PSFs, and fit the three components

<sup>5</sup> <http://www.stsci.edu/hst/observatory/focus/FocusModel>

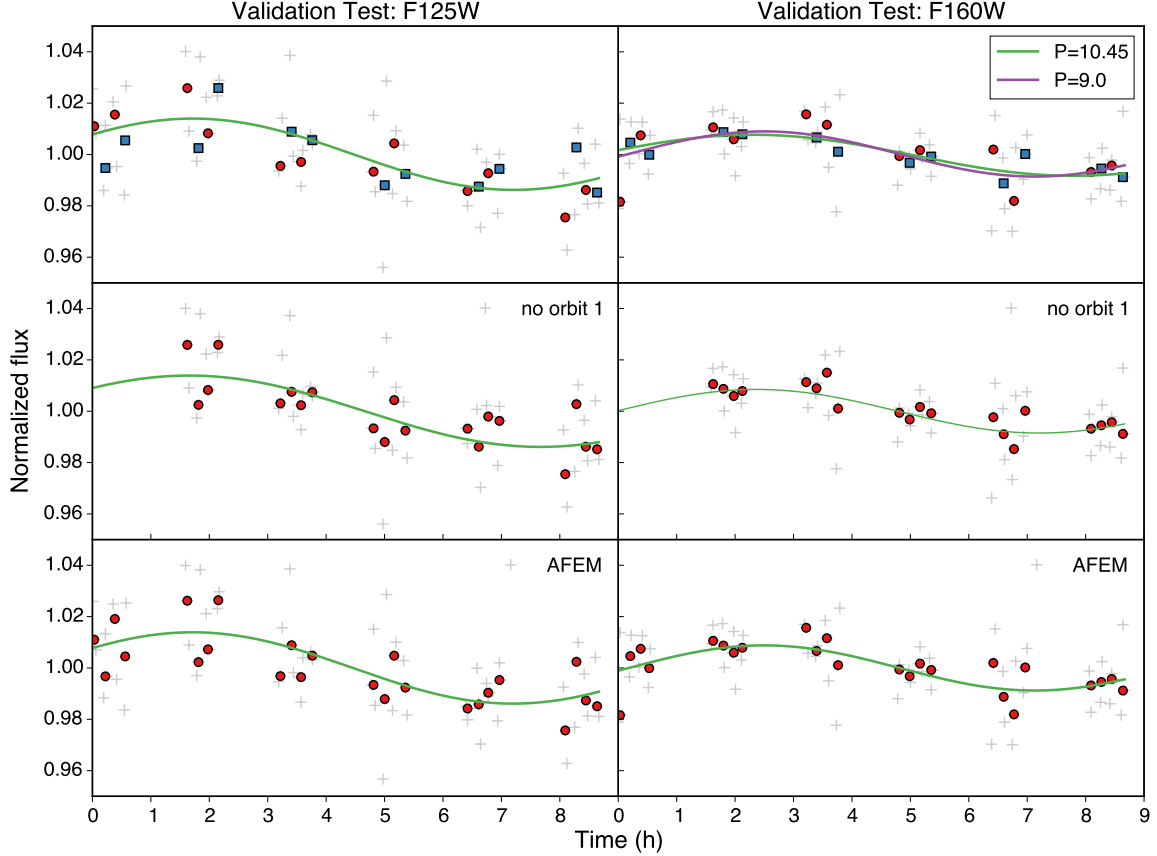


FIG. 2.— F125W (left) and F160W (right) light curves under different variability verification tests. Individual measurements are plotted with gray crosses. Photometric measurements of the same exposure sequence are binned, and binned photometry are plotted with points or squares. Best fitted sinusoidal curves are plotted with solid lines. *Upper*: binned measurements taken in dithering position 1 and 3 (red points) and that taken in 2 and 4 (blue squares) are plotted with different symbols. They demonstrate same trend of modulation. In upper left panel, green line is sinusoidal wave fitted with all parameter set free, and purple line is sinusoidal wave fitted with period set the same as that of F125W. *Middle*: sinusoidal waves fitted without using the data taken in Orbit #1. These curves are almost identical to the curves plotted in upper panel. *Lower*: photometry measured with AFEM-added images and best fitted sinus curves. These points and curves are also almost identical to those plotted in the upper panel.

together. We find that by introducing the correction term, the reduced  $\chi^2$  of PSF fitting is decreased from  $\sim 10$  to  $\sim 1$ . Relative photometry is acquired from the scaling parameters of the *Tiny Tim* PSFs.

PSF profiles change with exposure positions due to pixelation, especially for the case that WFC3 IR is significantly under-sampled. Also, the flat fields may potentially have large scale structures (Dressel 2012). We find a correlation of photometry with PSF positions on detector frame for both 2M1207 A and b. Correction is made by normalizing each group of exposures that have the same dithering position and telescope roll angle individually – we take the median of the fluxes that are measured from these exposures as normalization factors and divided them from every photometric measurement. Because the normalization factor for each group of exposures is calculated across the whole observation in time domain, this step has negligible impacts on variability analysis.

### 3.2. Uncertainty Analysis: White noise

First we estimated the photon noises for the photometry of 2M1207b. The total photon noise of the photometry is calculated by combining the photon noise of every single pixel that is calculated from count rates and de-

tector gain. The photon noises for photometry in F125W and F160W are 1.33% and 1.02%, respectively.

Since the PSFs for the 2M1207 A and b are fitted simultaneously, the uncertainties of photometry and position for the primary and secondary are coupled. Imperfection of position measurement of 2M1207 A could potentially significantly affects the photometry of 2M1207 b. We used a Monte Carlo (MC) method to evaluate the overall systematic of the PSF fitting. We applied the PSF photometry to images that were added with random Poisson noises and repeat the photometry procedure for 1000 times. From the distribution of the result, the uncertainties for F125W and F160W photometry are 1.34% and 1.12%, respectively. We conclude that the white noise of our observation is dominated by photon noise.

### 3.3. Uncertainty Analysis: Flat field uncertainties

2M1207 b were observed at 8 different spots on the detector (2 rolls  $\times$  4 dithering positions). Imperfect flat field correction can potentially introduce position-dependent differences in the count rates. The uncertainty of WFC3 IR pipeline flat field is typically  $\sim 1\%$  (Dressel 2012).

In PSF photometry, however, multiple pixels are fit-

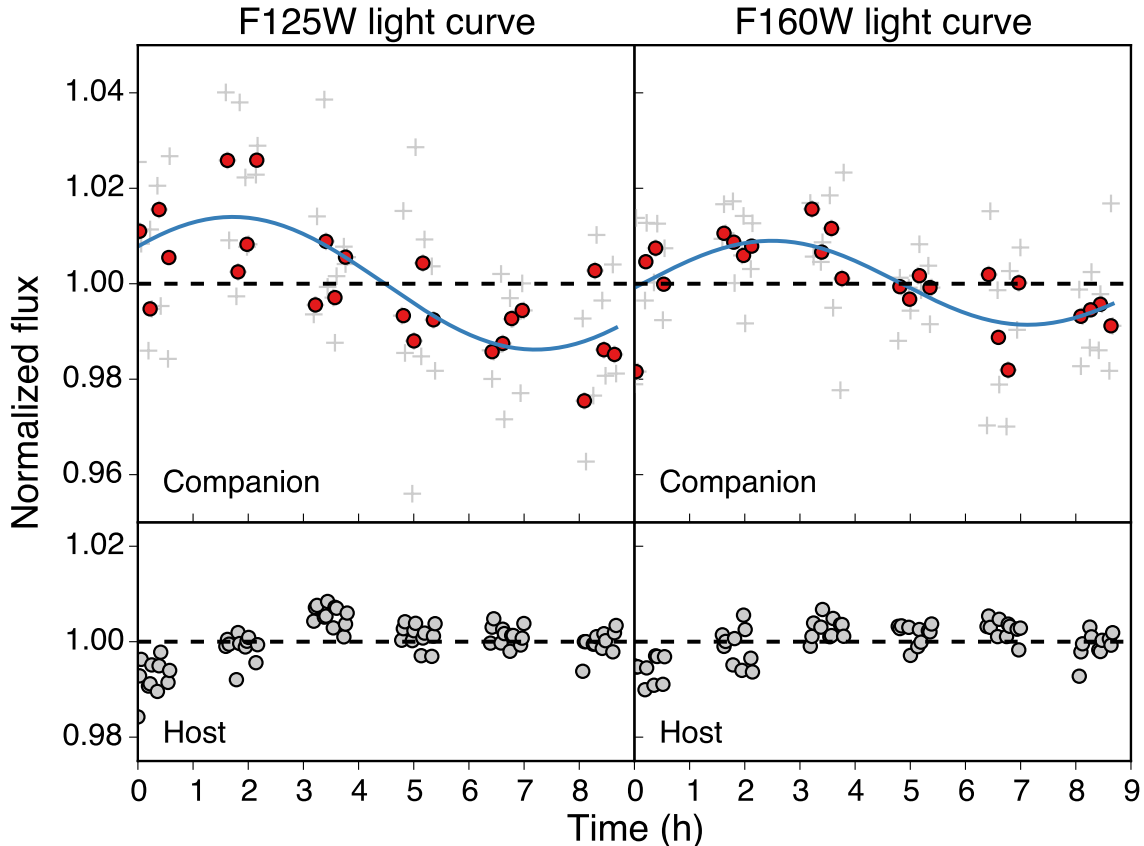


FIG. 3.— Normalized light curves for 2M1207 B (upper) and A (lower) with filter F125W (left) and F160W (right). Individual photometric measurement are plotted in gray crosses and binned photometry are plotted with red points. Best fitted sinusoidal waves are plotted with blue solid lines.

ted simultaneously and we expect to be less affected by high spatial frequency flat field noise, and a lower than 1% uncertainty from the flat field errors. To verify this, we multiplied every image by an artificial flat field error mask (AFEM) – a uniformly distributed Gaussian noise array with mean of 1 and sigma of 1% – and repeated the PSF photometry on the resulting images. The analysis of these experiments showed almost identical light curve to the original, verifying that the flat field errors do not affect our photometry significantly (Figure 2, bottom panel).

#### 4. VERIFICATION OF PHOTOMETRIC MODULATIONS AND AMPLITUDE ESTIMATE

##### 4.1. Tests and Verification

The light curves that result from our photometry show apparently sinusoidal modulations, discussed in more details in §5. To verify that these modulations are intrinsic to the object and not results of our data reduction procedures or due to instrumental changes, we carry out three different tests.

First, we fit sinusoids independently to the light curves of two filters to verify the similarity of the signal in the two bands (Figure 2, top panel). Inconsistent periods or light curve shapes would argue against a genuine signal. We find that the periods of the best fit sine waves are similar,  $10.5^{+1.2}_{-1.3}$ h for F125W and  $9.1^{+1.1}_{-1.0}$ h for F160W. These periods are roughly consistent within the

uncertainty. Furthermore, these periods are not close to any timescales over which HST or WFC3 are known to changes.

As a second test, we repeat the analysis neglecting the first orbit. The motivation behind this test is that, due to spacecraft thermal settling, the first orbits of HST observations are often slightly unstable, and neglected in high-precision studies (e.g. Mandell et al. 2013). Indeed, in our analysis 2M1207 A is significantly fainter in the first orbit (Figure 3) than in the subsequent ones. Our analysis based on orbits 2–6 finds essentially identical results to our analysis using the whole 6 orbits, based on which we conclude that the first less reliable orbit does not affect our results significantly (Figure 2, middle panel).

As a third test, we explore whether a subset of images, perhaps due to imperfectly normalized or correlated with specific instrument states, can drive the light curves into an apparently sinusoidal shape. To test this possibility, we split the data into two temporally overlapping halves: subset one are images taken at dithering position 1 and 3, and subset two are those taken at dithering position 2 and 4. For both data-sets, we repeated our analysis independently. For both of F125W and F160W, two halves demonstrated similar trend of variability. Our analysis detect sinusoidal modulations in *both* subsets and in *both* filters, with periods and amplitudes consistent with those derived from the complete data set (Figure 2, upper panel).

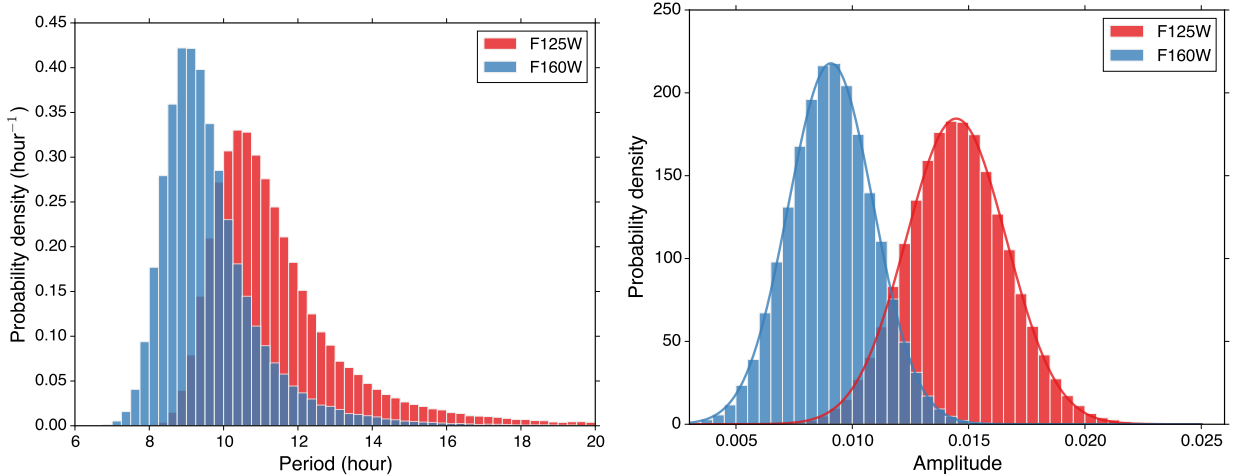


FIG. 4.— Distributions for periods (left) and amplitudes (right) for the light curve of F125W and F160W. The bin size for histograms of period is 0.25 hour and for that of amplitude is 0.5%. Histograms are normalized in the way that total area of the histogram equals to 1. In the right panel, Gaussian profiles are fitted to the histograms of periods and plotted in solid lines.

These tests demonstrate that the modulation seen in our data are consistently present in the different filters, in the different time segments of the data, and in data obtained in different dithering positions. All of the three tests support the modulation signal to be intrinsic to the target.

#### 4.2. Amplitude and Period Measurements

We use a MC method to analyze the light curve, and provide amplitudes and periods as well as their uncertainties for both filters. We generate series of random Gaussian noises with the standard deviation same as the photon noises, add them to the original light curves, and fit sinusoids to the newly combined light curves. We repeat above routine for 100,000 times and obtain the distribution of the fitting parameters (Figure 4).

### 5. RESULT

We present the first high-resolution, high-cadence, and high-precision photometry of a directly imaged planet or planetary-mass companion. Our observations reveal a modulation in the light curve of the  $\sim 4M_{\text{Jup}}$  companion 2M1207b, the first detection of modulations in directly imaged planetary mass objects. The best fitted periods for F125W and F160W are 10.5 and 9.1 hour, respectively. The modulation amplitudes for the normalized light curves are 1.45% and 0.92% for F125W and F160W light curves.

We obtain high signal to noise photometry series for both 2M1207 A and B (Figure 3). On average, the photometric contrast is  $6.52 \pm 0.01$  mag for F125W and  $5.77 \pm 0.01$  mag for F160W. The difference of F125W contrast from that measured in J-band (Mohanty et al. 2007) and F160W contrast from that measured with NICMOS F160W (Song et al. 2006) is due to the different throughput profiles of the filters.

The distributions for the periods demonstrate long tail shaped towards long period, with core region roughly Gaussian. With 64% confidence, we estimate the  $1-\sigma$  range for the periods of F125W and F160W to be  $10.5^{+1.3}_{-1.2}$  and  $9.1^{+1.1}_{-1.0}$  h, respectively. The period of best fitted sinusoid for F125W light curve is 1.5h longer than

that for F160W, which is  $\sim 20\%$  larger than  $1-\sigma$ . We also jointly fit the two band light curves forcing the periods of two sinusoids to be the same. We derive a modulation period of  $10.2^{+0.9}_{-0.8}$  h.

We discover that the modulation amplitudes in the two bands are significantly different. By fitting Gaussians to the MC fit result distributions, we determine that modulation amplitude of F125W is 1.45% with a standard deviation of 0.22%, and that of F160W is 0.92% with a standard deviation of 0.20%. The peaks of the two histograms separate by more than  $2-\sigma$ . The modulation amplitude for F125W is 1.58 times of that for F160W light curve.

### 6. DISCUSSION

A fundamental result of our study is the direct determination of the rotation period of a directly imaged planetary mass object. In the left panel of Figure 5 we compare the rotation period of 2M1207 b to the solar system planets,  $\beta$  Pic b the only other directly imaged planet with an estimated period and measured  $v \sin i$ , and field brown dwarfs from the study of (Metchev et al. 2015). The study by (Snellen et al. 2014) succeeded in measuring  $v \sin i$  for  $\beta$  Pic b and demonstrated that it fits a trend defined by Solar System planets in which more massive planets have faster rotation rates. The interesting finding that  $\beta$  Pic b, an exoplanet that formed in a protoplanetary disk, follows this trend suggests a possibly connection between planet mass, initial angular momentum, and formation in a disk.

Excitingly, our measurement of the rotation period of 2M1207b, a planet mass companion that has similar age to  $\beta$  Pic b, has a rotation period that fits in the same trend, as well as majority of brown dwarfs. We note that 2M1207 b is most likely formed in the same way as brown dwarfs by gravitational fragmentation. The result that objects formed in different scenarios share the same trend of period vs. mass suggests that rotation periods – in absence of well-determined ages – are not good tracers of the formation pathways and may not contribute important evidence for a formation in a disk vs. in a cloud core environment.



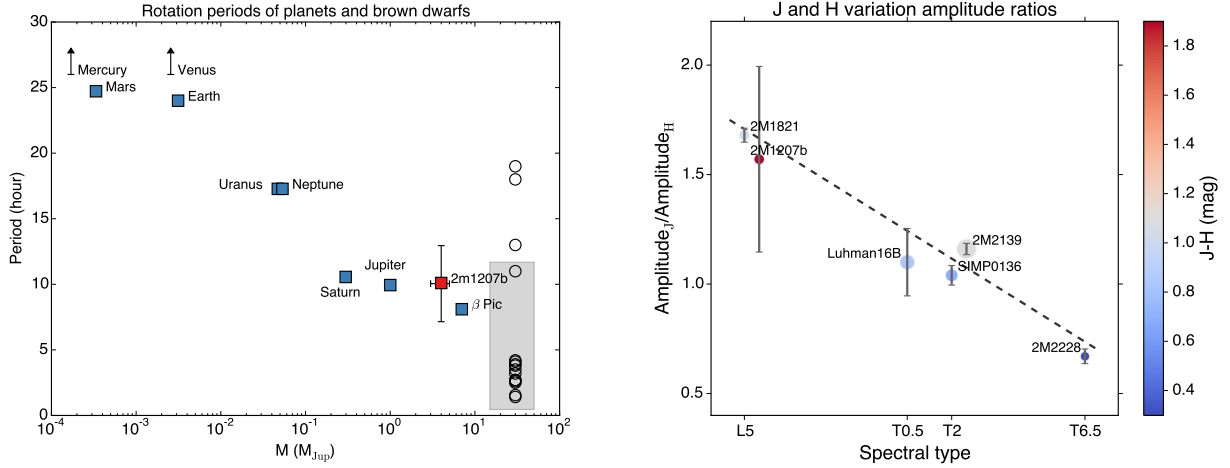


FIG. 5.— comparison of 2M1207’s rotation period and color change with brown dwarfs,  $\beta$  Pic b, and solar system planets. *Left*: period vs. mass plot for 2M1207 b (red square), solar system planets and  $\beta$  Pic b (blue squares), and brown dwarfs (black circles, gray shade). The mass of brown dwarfs are assumed to be  $30 M_{Jup}$ . The gray rectangle that has a  $\pm 15 M_{Jup}$  range in  $x$ , and a  $\pm \sigma$  of brown dwarf periods range in  $y$ , indicates a region where brown dwarfs most likely to appear in this diagram. Rotation period monotonically decreases with the increase of mass. *Right*: ratio of modulation amplitude in J and H band vs. spectral type for 2M1207b and brown dwarfs. The point for 2M1207 b is shifted to  $+x$  for half spectral type for clarification. The colors of the points represent J–H magnitude, and the sizes of the points are proportional to the J-band modulation amplitudes. The gray dashed line is the result of a linear fit to these points. Tight correlation of J- and H-band modulation amplitude ratio and spectral type is shown.

Furthermore, our observations allow us to compare the relative amplitudes in the J- and H-bands with the handful of brown dwarfs for which high-quality near-infrared time-resolved observations have been obtained. In the right panel of Figure 5, we compare the relative amplitude of J- and H-bands of 2M1207b and brown dwarfs (Apai et al. 2013; Buenzli et al. 2012, 2015; Burgasser et al. 2013; Radigan et al. 2012; Yang et al. 2014) that have different spectral types and J–H colors.

We find a tight correlation between the spectral type of the object and the J- to H-band modulation amplitude ratio. In the right panel of Figure 5, we demonstrate that earlier spectral type objects, independent of their surface gravity, have larger amplitudes at shorter wavelength than at longer wavelengths. Importantly, although the J–H color of 2M1207b is significantly redder, its relative modulation amplitude ratio is almost identical to the matching spectral type mid-L dwarf 2M1821.

This trend can be qualitatively explained using the toy model proposed in Yang et al. (2014) within the spectral type range of mid-L to L–T transition. Assuming that intensity modulations are introduced by a refractory cloud whose upper layer locates at altitude  $z$ , the variation amplitude ratio for J and H band can be expressed as  $Amp_J/Amp_H = \exp[-(\tau_J(z)/\tau_H(z))]$ , where  $\tau_J(z)$  and  $\tau_H(z)$  are the optical depths of upper cloud layer for J and H bands. The opacity for J band is smaller than that for H, therefore from mid-L to L–T transition, as the cloud upper boundary appears higher in the atmosphere, the optical depth difference for the two bands gets smaller, and the amplitude ratio decreases. We note, that the late T dwarf 2M2228 falls exactly on this trend, but whose variations are likely to emerge from a different mechanism as their silicate clouds are below the visible photosphere (e.g. Stephens et al. 2009).

We infer that the upper cloud layer of 2M1207b is at a similar optical depth as that of a matching spectral type field brown dwarf from the fact that they share similar J- and H-bands light curve amplitude ratio. The two processes that atmosphere opacity at certain pressure level enhances and the cloud thickness increases with the decrease of surface gravity have to counterbalance with each other to maintain the optical depth of the cloud upper layer.

## 7. CONCLUSIONS

In summary, from our J- and H-band high precision, high-cadence light curves we discovered sinusoidal modulations in the planetary mass object 2M1207b. This is the first detection of rotational modulations in a directly imaged planetary mass object. The period is  $10.2^{+0.9}_{-0.8}$ , similar to that derived from  $v \sin i$  measurements for the direct imaged exoplanet  $\beta$  Pic b and significantly longer than most field brown dwarfs with known rotation periods. The modulation amplitude ratio of J and H band is almost identical to one matching spectral type L5 dwarf, although they have very different J–H colors.

Finally, we note that the observations presented here open an exciting new window on directly imaged exoplanets and planetary-mass companions. Our study demonstrates a successful application of high-cadence, high-precision, high-contrast photometry with planetary mass companion. We also show that these observations can be carried out simultaneously at multiple wavelengths, allowing us to prove multiple pressure levels. With observation of a larger sample and at multiple wavelengths, we will be able to explore the detailed structures of atmospheres of directly imaged exoplanets, and identify the key parameters that determine these.

## REFERENCES

- Ackerman, A. S. & Marley, M. S. 2001, *ApJ*, 556, 872  
 Allard, F., Homeier, D., & Freytag, B. 2012, *Royal Society of London Philosophical Transactions Series A*, 370, 2765

- Apai, D., Radigan, J., Buenzli, E., Burrows, A., Reid, I. N., & Jayawardhana, R. 2013, *ApJ*, 768, 121
- Barman, T. S., Macintosh, B., Konopacky, Q. M., & Marois, C. 2011, *ApJ*, 733, 65
- Berta, Z. K., Charbonneau, D., Désert, J.-M., et al. 2012, *ApJ*, 747, 35
- Biretta, J. 2014, *Space Telescope WFC Instrument Science Report*, 1, 10
- Bonnefoy, M., Chauvin, G., Lagrange, A.-M., Rojo, P., Allard, F., Pinte, C., Dumas, C., & Homeier, D. 2014, *A&A*, 562, A127
- Buenzli, E., Apai, D., Morley, C. V., Fplateau, D., Showman, A. P., Burrows, A., Marley, M. S., Lewis, N. K., & Reid, I. N. 2012, *ApJ*, 760, L31
- Buenzli, E., Saumon, D., Marley, M. S., Apai, D., Radigan, J., Bedin, L. R., Reid, I. N., & Morley, C. V. 2015, *ApJ*, 798, 127
- Burgasser, A. J., Sheppard, S. S., & Luhman, K. L. 2013, *ApJ*, 772, 129
- Burrows, A., Sudarsky, D., & Hubeny, I. 2006, *ApJ*, 640, 1063
- Chauvin, G., Lagrange, A.-M., Dumas, C., Zuckerman, B., Mouillet, D., Song, I., Beuzit, J.-L., & Lowrance, P. 2005, *A&A*, 438, L25
- Dressel, L. 2012, *Wide Field Camera 3, HST Instrument Handbook*, 1
- Helling, C., Ackerman, A., Allard, F., Dehn, M., Hauschildt, P., Homeier, D., Lodders, K., Marley, M., Rietmeijer, F., Tsuji, T., & Woitke, P. 2008, *MNRAS*, 391, 1854
- Kimble, R. A., MacKenty, J. W., O’Connell, R. W., & Townsend, J. A. 2008, in *Society of Photo-Optical Instrumentation Engineers (SPIE) Conference Series*, Vol. 7010, *Society of Photo-Optical Instrumentation Engineers (SPIE) Conference Series*, 1
- Kostov, V. & Apai, D. 2013, *ApJ*, 762, 47
- Kreidberg, L., Bean, J. L., Désert, J.-M., et al. 2014, *Nature*, 505, 69
- Krist, J. 1995, in *Astronomical Data Analysis Software and Systems IV*, Vol. 77, 349
- Mandell, A. M., Haynes, K., Sinukoff, E., et al. 2013, *ApJ*, 779, 128
- Marley, M. S., Saumon, D., & Goldblatt, C. 2010, *ApJ*, 723, L117
- Marois, C., Macintosh, B., Barman, T., Zuckerman, B., Song, I., Patience, J., Lafrenière, D., & Doyon, R. 2008, *Science*, 322, 1348
- Metchev, S. A., Heinze, A., Apai, D., Fplateau, D., Radigan, J., Burgasser, A., Marley, M. S., Artigau, E., Plavchan, P., & Goldman, B. 2015, *ApJ*, 799, 154
- Mohanty, S., Jayawardhana, R., Huelamo, N., & Mamajek, E. 2007, *ApJ*, 657, 1064
- Patience, J., King, R. R., De Rosa, R. J., & Marois, C. 2010, *A&A*, 517, A76
- Radigan, J., Jayawardhana, R., Lafrenière, D., Artigau, E., Marley, M., & Saumon, D. 2012, *ApJ*, 750, 105
- Skemer, A. J., Close, L. M., Szűcs, L., Apai, D., Pascucci, I., & Biller, B. A. 2011, *ApJ*, 732, 107
- Skemer, A. J., Hinz, P. M., Esposito, S., Burrows, A., et al. 2012, *ApJ*, 753, 14
- Snellen, I. A. G., Brandl, B. R., de Kok, R. J., Brogi, M., Birkby, J., & Schwarz, H. 2014, *Nature*, 509, 63
- Song, I., Schneider, G., Zuckerman, B., Farihi, J., Becklin, E. E., Bessell, M. S., Lowrance, P., & Macintosh, B. A. 2006, *ApJ*, 652, 724
- Stephens, D. C., Leggett, S. K., Cushing, M. C., Marley, M. S., Saumon, D., Geballe, T. R., Golimowski, D. A., Fan, X., & Noll, K. S. 2009, *ApJ*, 702, 154
- Yang, H., Apai, D., Marley, M. S., Saumon, D., Morley, C. V., Buenzli, E., Artigau, E., Radigan, J., Metchev, S., Burgasser, A. J., Mohanty, S., Lowrance, P. J., Showman, A. P., Karalidi, T., Fplateau, D., & Heinze, A. N. 2014, *ApJ*, 798, L13